Lab on a Chip

PAPER

View Article Online
View Journal | View Issue

Cite this: *Lab Chip*, 2023, **23**, 4033

Sample preconcentration through airjet-induced liquid phase enrichment†

Edward Wang, [a] Louise C. Laurent,[b] Drew A. Hall[c] and Yu-Hwa Lo*[ac]

Sample preparation is essential for nucleic acid assays, affecting their sensitivity and reliability. However, this process often results in a significant loss or dilution of the analyte, which becomes a bottleneck that limits downstream assay performance, particularly for assays that accept a limited input sample volume. To overcome this challenge, we present an evaporative-based sample enrichment method that uses an airjet to concentrate analytes within a small, defined volume by reversing the coffee-ring effect. A small, concentrated sample can then be collected for analysis to increase the initial sample load. The effectiveness of the reported airjet enrichment was quantified using qPCR of λ-DNA, HeLa-S3 RNA, and heat-inactivated SARS-CoV-2 samples. Comparisons between airjet enrichment and conventional evaporative concentration methods demonstrated significant advantages of airjet enrichment, including the ability to concentrate a high percentage of analyte within a 1 μL volume. The enrichment method was then integrated and adapted for various fluid volumes commonly found in nucleic acid sample preparation procedures. Here, airjet enrichment reduced the overall C_q by an average of 9.27 cycles for each analyte, resulting in a 600-fold enrichment from the initial concentration. To perform selective enrichment and prevent salt-based interference in downstream analysis, PEG was added to reduce the co-enrichment of salt. In addition, a preliminary study was conducted to explore the integration of airjet enrichment into ELISA using rabbit IgG as a model antigen. These findings demonstrate how airjet enrichment can be easily integrated into existing laboratory protocols with minimal modification and significantly improve the performance of biosensors.

Received 4th June 2023,
Accepted 16th August 2023

DOI: 10.1039/d3lc00481c

rsc.li/loc

Introduction

The analytical sensitivity of assays is heavily influenced by upstream sample preparation steps,[1,2] and by the signal generation, amplification, and detection mechanisms that follow. Significant advancements in detection schemes for various biosensors have been reported,[3,4] yet progress in sample enrichment and pre-treatment has been slower. A major challenge with sample preparation is the loss and/or dilution of analyte that occurs during the transfer, washing, and elution steps. Elution of the purified nucleic acid into a relatively large (typically 50–100 μL) volume of elution buffer for analysis using an assay that accepts a small (typically 1–5 μL) sample input volume will itself result in a low (1–10%) sample transfer efficiency, without even considering the many intermediate transferring and washing steps before elution. The low efficiencies of the majority of sample preparation workflows represent a sensitivity bottleneck in current biosensors for *in vitro* diagnostics (IVD). To address this challenge, we developed a sample processing method to concentrate the analytes within a small volume (1–2 μL) to be transferred for downstream analysis. In addition, our liquid-phase sample enrichment method provides a certain degree of selectivity to suppress the simultaneous concentration of extraneous solutes that may interfere with downstream analytical processes. This method can be widely applied to various biosensors regardless of the analyte type or signal generation, amplification, or detection methods.

Many sample preconcentration techniques have been reported using the properties of solid-phase affinity,[5,6] liquid-phase affinity,[7,8] and electrophoresis.[9–11] However, these heavily depend on the analyte's charge, surface binding affinity, or solvent miscibility for optimal effectiveness. Conceptually, the most straightforward preconcentration method that is analyte independent is solvent removal by evaporation.[12,13] As most analytes in biosensors are non-volatile, the volume reduction caused by evaporation

[a] *Department of Aerospace and Mechanical Engineering, Materials Science and Engineering Program, University of California, San Diego, La Jolla, CA, USA. E-mail: ylo@ucsd.edu*
[b] *Department of Obstetrics, Gynecology, and Reproductive Sciences, University of California, San Diego, La Jolla, CA, USA*
[c] *Department of Electrical and Computer Engineering, University of California, San Diego, La Jolla, CA, USA*

† Electronic supplementary information (ESI) available. See DOI: **https://doi.org/10.1039/d3lc00481c**

increases the analyte concentration. However, this simple approach has shown limited success to date due to the well-known coffee-ring effect (CRE), where the analytes and all other non-volatile species, including salts, precipitate on the dry surface in a random pattern as the liquid volume is reduced by evaporation. While some works claim that the coffee-ring patterns mark the distributions of the analytes that may facilitate resuspension or *in situ* detection,[14] the CRE is generally an undesirable effect that compromises sensitivity, reproducibility, and operability for IVD,[15] and as a result, significant efforts have been made to overcome the formation of coffee rings and to keep analytes in liquid solution.[16,17]

An evaporating droplet forms a differential evaporative gradient, having the highest evaporation rate at the droplet's perimeter. This evaporation rate gradient induces a radially outward flow to drive fluid within the droplet toward the periphery to replenish the lost fluid at the liquid–solid interface. As a result, any solutes or suspended particles are carried to the contact line and deposited.[18,19] CRE reversal can be achieved through electroosmosis,[20] electrowetting,[21,22] surface wave acoustics,[23,24] infrared laser heating,[25] or microfabricated surface patterning.[26,27] However, these processes are generally complicated and depend on the properties of the particles, such as particle size, charge, hydrophobicity, *etc.* Above all, with or without CRE, any evaporation method enriches not only the analytes but also the other solutes in the buffer, such as salts, which can interfere with downstream analysis.

This work demonstrates an effective sample enrichment method to reverse the CRE and keep all analytes in the liquid during an accelerated evaporation process, confine the analytes in a well-defined area on the liquid surface for easy collection and transfer by a pipette, and achieve a certain level of selectivity to minimize co-enrichment of salt and other small molecular species besides the analytes. The core concept is to use airjet-induced evaporation to reverse the coffee-ring flow. The airflow drives analytes from a relatively large sample volume towards a small region under the airjet. Coffee-ring flow reversal is achieved by aiming the nozzle perpendicular to the liquid surface and initiating the airjet to increase local evaporation. The localized increase in evaporative flux establishes a differential evaporative gradient and induces fluid flows toward the area to replenish the lost liquid. During this process, the flow carries dissolved molecules or suspended particles, which become highly concentrated in a small, localized area underneath the nozzle. The method has a simple setup: a compressed air source, an air heater, and the airjet nozzle. In addition, a small amount of surfactant (*e.g.*, methyl cellulose) is added to the sample to suppress fluid turbulence.

We demonstrate the effectiveness by concentrating a range of particles and biological analytes including proteins and nucleic acids. Spiked samples containing rabbit IgG, λ-DNA, HeLa-S3 RNA, and heat-inactivated SARS-CoV-2 were used as model analytes. Enhanced performance in ELISA and the reduction in cycle threshold value (C_q) in PCR analysis was used to quantify analyte enrichment and collection efficiency. Polyethylene glycol (PEG) was mixed with the sample to minimize potential adverse effects on downstream reactions (*e.g.*, PCR) due to the co-concentration of salt and other non-volatile components since PEG forms a matrix under the airjet to reduce salt accumulation. The airjet enrichment method was employed in microfluidic and mesofluidic systems to handle sample volumes from <100 μL to >1 mL and cover the range of sample volumes used in common laboratory workflows upstream PCR-based detection. The approach addresses the bottleneck in sample preparation by significantly increasing the analyte collection efficiency, up to a few hundred times more than current practices. This increase in efficiency can improve the sensitivity and repeatability of biosensing and IVD assays.

Materials and methods

Reagents

Methyl cellulose (M7140), rabbit IgG (15006), goat anti-rabbit IgG (R2004), TMB (T0440), bovine serum albumin (A7906), PEG_{400} (202398), and EDTA disodium salt (E5134) were purchased from MilliporeSigma. Anti-rabbit IgG antibody conjugated with HRP (PI-1000-1) was purchased from VectorLabs. Carboxylate-modified 1um beads (T8883), streptavidin conjugated quantum dots (Q10143MP), λ-DNA (SD0011), and HeLa-S3 total RNA (AM7852) were purchased from Thermo-Fisher Scientific. Heat-inactivated SARS-CoV-2 (VR-1986HK) were purchased from ATCC. FITC-labeled oligonucleotides and primers for λ-DNA, *BRACA1*, and *N1* were synthesized by Integrated DNA Technologies (IDT). For PCR analysis, iTaq Universal SYBR Green Supermix (1725120) and iTaq Universal SYBR Green One-Step Kit (1725150) were purchased from BioRad.

Fabrication of nichrome heater

A borosilicate glass Pasteur pipette was separated into two halves. A coil from 40 mm of 28-gauge nichrome wire was made, and the ends were braided with electrical wire. After the coil was inserted into the pipette half, the other half was re-sealed using a heat-resistant ceramic adhesive. The ends of the wire were connected to an adjustable DC voltage supply (Tekpower TP1503C) during operation.

Airflow evaporation on a sessile droplet

Glass slides were treated under UV-Ozone (Jelight Model 42) for 10 minutes. A section of cured PDMS with a 14 mm hole punched through the center was then pressed on the glass surface for a minute before removal to create a hydrophobic barrier. Solutions of the respective analyte were mixed in ultrapure H_2O containing 50 μg mL^{-1} methyl cellulose. 20 μL of the respective solution for enrichment was deposited on the hydrophilic section of the cover slip. The airjet nozzle

was placed 5 mm from the droplet surface and run for the designated time.

Temperature profiles for the nichrome airflow heater

A thermal camera (FLIR A300) was used to capture thermal images for the nichrome heater and liquid in a 96-well plate. A solution of dye and 50 μg mL^{-1} methyl cellulose in ultrapure H_2O was used as the bulk liquid and filled the well. The airflow rate and the voltages were adjusted accordingly. 3 minutes were given to achieve steady state before taking the temperature profile. The current through the circuit was measured to determine the power.

Enrichment in a 96-well plate for DNA and RNA

The wells were treated with 200 μL of Rain-X for 5 minutes, washed twice with water, and dried prior to enrichment studies. Solutions containing dilutions of λ-DNA and 1 : 1000 HeLa-S3 total RNA were prepared in ultrapure H_2O. Methyl cellulose was added to bring the concentration to 50 μg mL^{-1} in addition to dilute tracking dye. For the reference sample, 1 μL of each solution was transferred directly to a qPCR mixture with 10 μL of total volume. The λ-DNA was enriched under the nichrome at a voltage of 3.25 V and an airflow rate of 1.00 slpm. The enrichment was continued until the liquid height reached 10% of the original height, and a concentrated dye spot formed. Upon completion, 1 μL of fluid was extracted from the concentrated dye spot using a micropipette and deposited into a qPCR mix. The HeLa-S3 RNA solution was performed similarly, except the airflow rate was reduced to 0.75 slpm when the liquid height reached 25% of the initial height.

Double-stage enrichment

To create the large volume container, the tops of a 15 mL falcon tube were cut off at the 2.5 mL mark, and the bottom half was saved. A circular piece of foil containing an 8 mm hole in the center was then adhered to the top of the tube. Solutions of diluted λ-DNA, HeLa-S3 RNA, and heat-inactivated COVID-19 particles were made in ultrapure H_2O containing a small amount of tracking dye. In the cut tube, 2 mL of each solution was added. The ends of a pipette tip were trimmed, and the tip was placed in the hole. The nichrome nozzle was placed in the interior of the pipette tip and set at a flow of 2.0 slpm at a voltage of 7.5 V. The enrichment was performed until 1 mL evaporated off and a distinct layer of concentrated dye formed. The enrichment in the 96-well plate was performed as previously described, adding 1 μL of 5 mg mL^{-1} methyl cellulose to the well to achieve spot enrichment. After enrichment in the large volume and 96-well containers, 1 μL of the enriched sample was transferred to a qPCR reaction and compared with 1 μL of the reference sample from the initial nucleic acid solution. Negatives were run simply based on evaporation, where the inner tube was not present for the large volume enrichment, and no methyl cellulose was present in the 96-well enrichment. Fold enrichment values of each nucleic acid was calculated according to its amplification efficiency (Fig. S1†).

Buffered enrichment using PEG

Similar solutions of λ-DNA, 1 : 1000 HeLa-S3 RNA, and 1 : 500 of ATCC heat-inactivated COVID-19 particles were made in 0.1 mM EDTA with a small amount of blue tracking dye. The respective solutions were transferred to the large-volume container and evaporated similarly to the original series enrichment. After forming the enriched layer, 100 μL was collected and deposited in a 96-well plate. In each individual well, 1 μL of 5 mg mL^{-1} methyl cellulose and 5 μL of PEG_{400} were mixed to form a homogenous solution. The enrichment was run according to the previous 96-well plate protocol.

ELISA enrichment

A 96-well plate was incubated with 100 μL of 20 μg mL^{-1} of goat anti-rabbit IgG overnight at 4 °C. The wells were then washed two times with wash buffer (0.05% Tween-20 in 1X PBS) before adding 300 μL of 1% BSA and incubating for 1 hour at room temperature (RT). Separately, 100 μL of rabbit IgG dilutions in 1X PBS and dilute dye were added to a 96-well plate with 1 μL of 5 mg mL^{-1} of methyl cellulose mixed in for the enriched samples. The dilutions were placed under the airjet with a wattage of 1.9 W and flow speed of 0.1 sl min^{-1}, until 10 μL remained in the well. Enrichment was determined through the co-enrichment of the dye. Upon completion, 1 μL was withdrawn from the center and re-diluted in 99 μL of 1X PBS. This solution was deposited in the well containing the capture antibody and incubated for 1 hour shaking at RT. The wells were washed two times with wash buffer and 100 μL of a 1 : 1000 dilution of HRP-conjugated goat anti rabbit IgG was added. The solution was incubated for 1 hour at RT before being washed four times with wash buffer and adding 100 μL of TMB to the wells. Resulting images were captured on a smartphone and analyzed under ImageJ to determine color intensity.

Results and discussion

Using an airjet to reverse the coffee ring effect (CRE)

The operating principle for airjet enrichment is depicted in Fig. 1, which illustrates the particle distribution under ambient evaporation and airjet enrichment in a sessile droplet. The development of the CRE has been attributed to the non-uniform evaporative profile across the droplet's surface. The evaporative flux is greatest at the contact line for ambient evaporation because it represents a large proportion of the liquid–air interface.[28] As a result, an evaporative gradient is established at the droplet periphery, and a radially outward flow is formed from the interior to replenish the lost fluid. This flow carries any solutes or suspended particles toward the contact line, forming a familiar ring-like pattern.

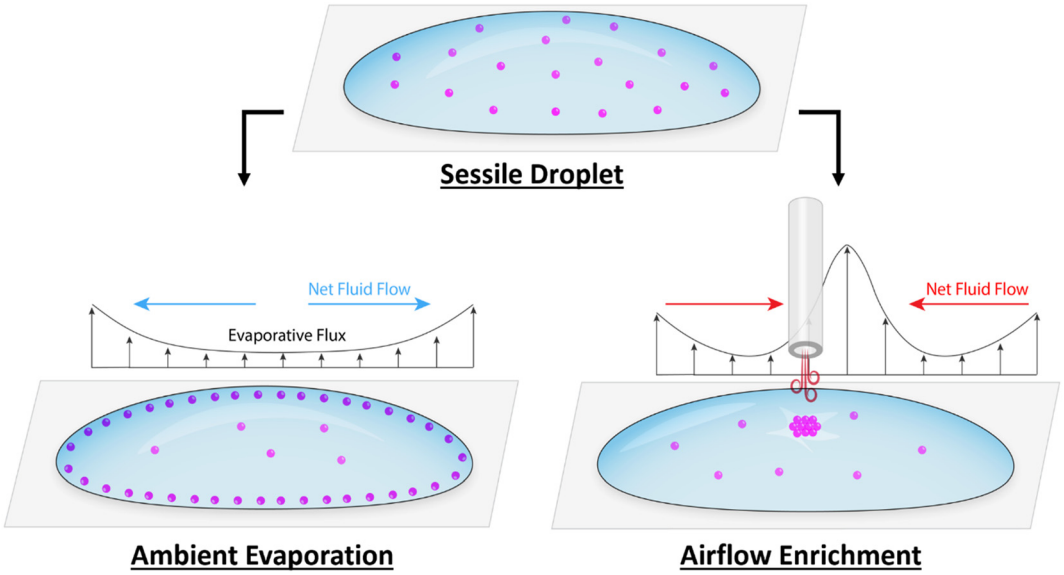

Fig. 1 Schematic of airjet enrichment to reverse coffee-ring flows and the comparison of the resulting deposition patterns with that of ambient evaporation.

Airjet enrichment reverses this radial flow by establishing a large evaporative flux at the center of the droplet by positioning a nozzle above the droplet and directing a jet of air perpendicular to its surface. The airjet displaces the boundary layer comprised of saturated water vapor, which lies directly above the liquid–air interface. Displacement of the boundary layer leads to enhanced diffusion across the interface[29,30] and shifts the evaporative gradient towards the area under the airjet. In addition, as the speed of enrichment is heavily dependent on the evaporation rate, the temperature of the airjet can be used to control the overall evaporation rate.

Suppression of airjet-induced turbulence

In a previous study,[31] we explored airjet enrichment in microfluidic paper-based devices exhibiting characteristic laminar flow behavior. However, achieving laminar flow in

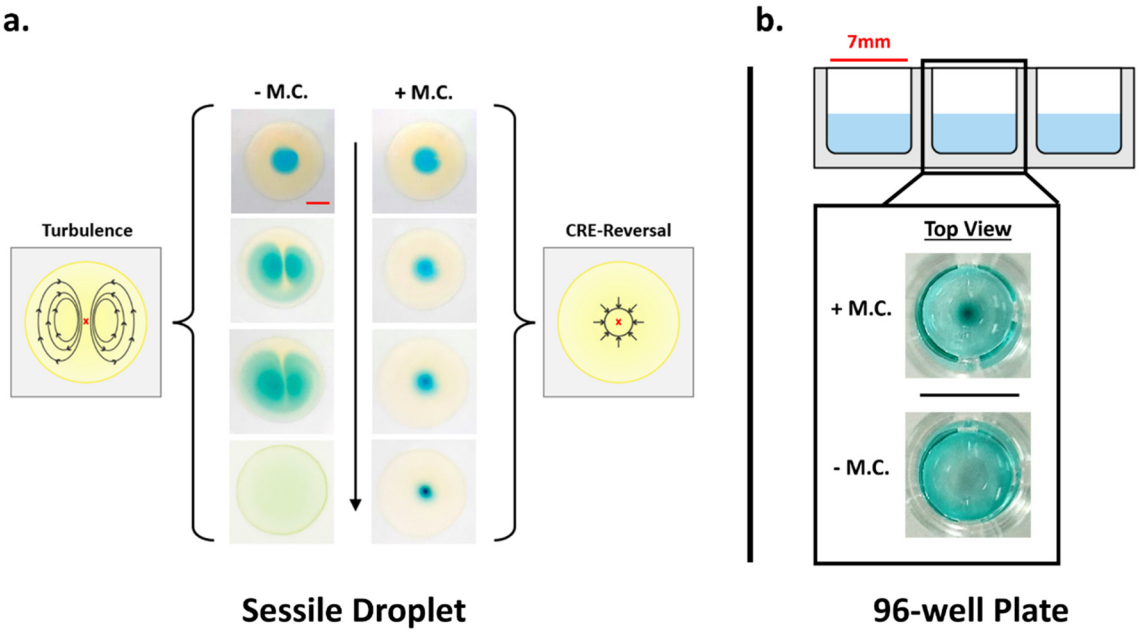

Fig. 2 (a) Images of fluid behavior under an airjet in the absence (– M.C.) and presence (+ M.C.) of the methyl cellulose surfactant in a droplet as the process progresses (from top to bottom). Scale bar: 4 mm. (b) Images from a 96-well plate after enrichment with (+ M.C.) and without (– M.C.) methyl cellulose.

liquids can be challenging during enrichment, as the airjet inevitably imparts shear forces on the liquid surface, leading to turbulent motion that disrupts the radial flow induced by evaporation. An additive is required to stabilize the surface and suppress streaming and turbulence to achieve the desired enrichment effect. The additive used in this study is methyl cellulose, a relatively inert and biocompatible component with surfactant-like properties. Fig. 2a demonstrates how the presence of methyl cellulose mitigates the airjet-induced secondary flows to achieve a condensed spot through CRE reversal. In a 20 μL sessile droplet, which has been dyed yellow, a region of blue dye was added to visualize liquid movement. Without methyl cellulose, turbulent, vortical flow patterns quickly develop within the droplet upon initiating the airjet. This leads to increased mixing between the blue and yellow dye, eventually forming a uniformly green solution. However, by adding methyl cellulose to the droplet, the turbulent patterns are suppressed and evaporative-driven, radial flow dominates, as indicated by the increasingly concentrated blue region of the dye.

Similar behavior was also observed for fluid in a 96-well plate (Fig. 2b). In individual wells, 100 μL of a blue dye solution was deposited and evaporated underneath the airjet. A clear enrichment spot of concentrated dye was formed for solutions containing methyl cellulose, while solutions lacking methyl cellulose had the dye evenly distributed throughout the entire process. In solutions which contained an enrichment spot, the entirety of the spot could be collected within 1 μL of volume. The presence of methyl cellulose is critical to the enrichment process, and its addition allows enrichment to occur in various fluid containers.

The mechanism in which methyl cellulose can suppress the airjet-induced fluid flows is attributed to its surfactant properties. Surfactants have been shown to reduce wave activity in liquids through the Gibbs–Marangoni effect.[32] Here, the formation of capillary waves is attenuated as they would produce localized variations in surfactant density at the liquid–air interface and consequently lead to counteracting surface-tension gradients. However, not all surfactants screened during this study could completely inhibit the airjet-induced turbulence to the same degree as methyl cellulose. Therefore, additional properties are likely to play a role in the effectiveness of surface stabilization. While this study focuses on enrichment in aqueous solutions, we have also successfully performed enrichment on volatile organic solvents such as ethanol using PDMS as the surfactant (Fig. S2†). Continued exploration of surfactants and their effects on a variety of solvents will therefore yield more insight into the optimal properties required for airjet enrichment.

Ubiquitous enrichment

Fig. 3 shows that airjet enrichment can effectively improve detection sensitivity and concentrate various fluorescent biomacromolecules and particles, regardless of size. Solutions containing FITC-tagged DNA oligonucleotides, green fluorescent protein (GFP), streptavidin-functionalized quantum dots, and 1 μm fluorescent beads were deposited on a hydrophilic glass slide. Methyl cellulose was added to the droplet to prevent fluid turbulence caused by airflow. A glass pipette with a 1.5 mm I.D. exit nozzle was then used to create an airjet. The air was provided by a nitrogen tank and the strength of the airjet was controlled by a digital mass flow meter. For each solution, the fluorescent particles were concentrated to a defined spot of 300–500 μm in diameter underneath the airjet. The results in Fig. 3 demonstrate the broad applicability of this method for enriching all types of components in a liquid, independent of their physical and chemical properties.

Influence of a heated airjet on liquid temperatures

The speed of the enrichment process depends on the evaporation rate underneath the airjet. To reduce evaporation times, a heating element consisting of a nichrome coil was

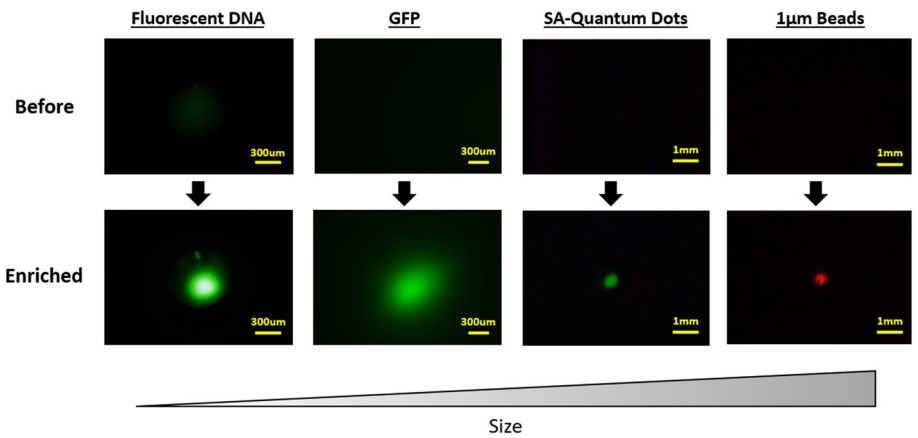

Fig. 3 Images before and after enrichment with equal exposure time for FITC-tagged DNA oligonucleotides, green fluorescent protein (GFP), streptavidin-functionalized quantum dots, and 1um fluorescent beads.

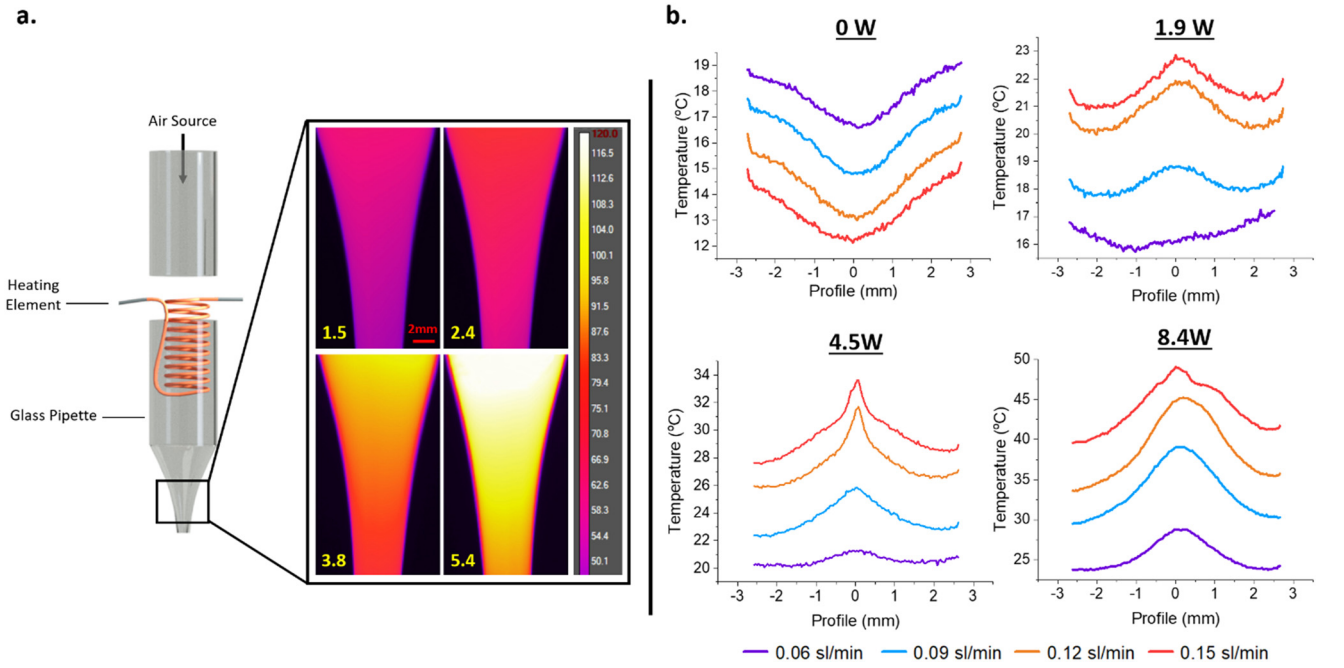

Fig. 4 (a) Scheme of the heated airjet and associated thermal images taken at specific wattages (yellow values) corresponding to applied voltages of 3, 4, 5 and 6 V respectively. (b) Temperature profiles of the liquid surface for different wattages and airflow speeds.

inserted and sealed in the glass pipette and connected to a variable voltage source (Fig. S3†). An infrared camera then measured the temperature profiles near the pipette's exit nozzle at different voltages with a constant airflow rate of 1.0 standard liter per minute (sl m^{-1}) (Fig. 4a). A linear relationship between the power and mean surface temperature was established (Fig. S4†), allowing for control over the airjet temperature.

To avoid damaging biological-based analytes that are vulnerable to denaturation or degradation at high temperatures,[33,34] the surface temperature profile of the liquid was also measured by the infrared camera under different airjet flow rates and temperatures. Fig. 4b shows the surface temperature profiles of a liquid solution in a 96-well plate. When the nichrome heater is turned off (0 W), greater airflow rates give rise to lower temperature minimums due to evaporative cooling[35] and quicker boundary layer displacement. However, this trend is reversed in power values greater than 1.9 W to the heating element, whereby faster airflow rates cause higher peak temperatures through increased levels of heat transfer. However, a power under 4.5 W did not increase the temperature above 35 °C, as shown in the temperature readings in Fig. 4a, and therefore represented an upper limit to minimize degradation of biological analytes.

For the measured temperature profile at 0 W, a negative temperature gradient can give rise to inward Marangoni flows due to the temperature dependence of surface tension in the liquid.[16] In previous reports, Marangoni flows have suppressed the CRE by establishing a similar surface tension gradient through temperature differences or surfactants.[36,37] By controlling the heater temperature in the air path, we can control the temperature profile of the liquid surface and achieve an almost isothermal profile. Since the effect of enrichment was observed under different temperature profiles, it can be concluded that the dominant effect responsible for analyte enrichment is the increased localized evaporation rate by the airjet, while the surface-tension-induced Marangoni flows play only a minor role. Therefore, the primary parameters we choose in the following experiments will be air flow rate and air heating to achieve high enrichment efficiency within a short time and preserve the properties of the analytes for the downstream process.

Double-stage enrichment for varying sample volumes

Incorporating airjet enrichment into the upstream steps of analyte detection can significantly improve the overall sensitivity. A model workflow was developed to demonstrate how airjet enrichment can be integrated to accommodate the fluid volumes typically used in these detection procedures (Fig. 5a). The model comprises two stages of fluid processing, each corresponding to a range of fluid volumes that can be enriched. The first stage is the large volume enrichment stage, which can enrich mesofluidic volumes (mLs), followed by the small volume enrichment stage for enriching microfluidic volumes (μLs). Each step is optimized to balance enrichment speed and effectiveness to maximize the overall concentration of analyte prior to analysis.

The large volume enrichment stage can typically process 1–3 mL of fluid, emphasizing maximizing the evaporation rate. This stage has a key component – inserting an inner

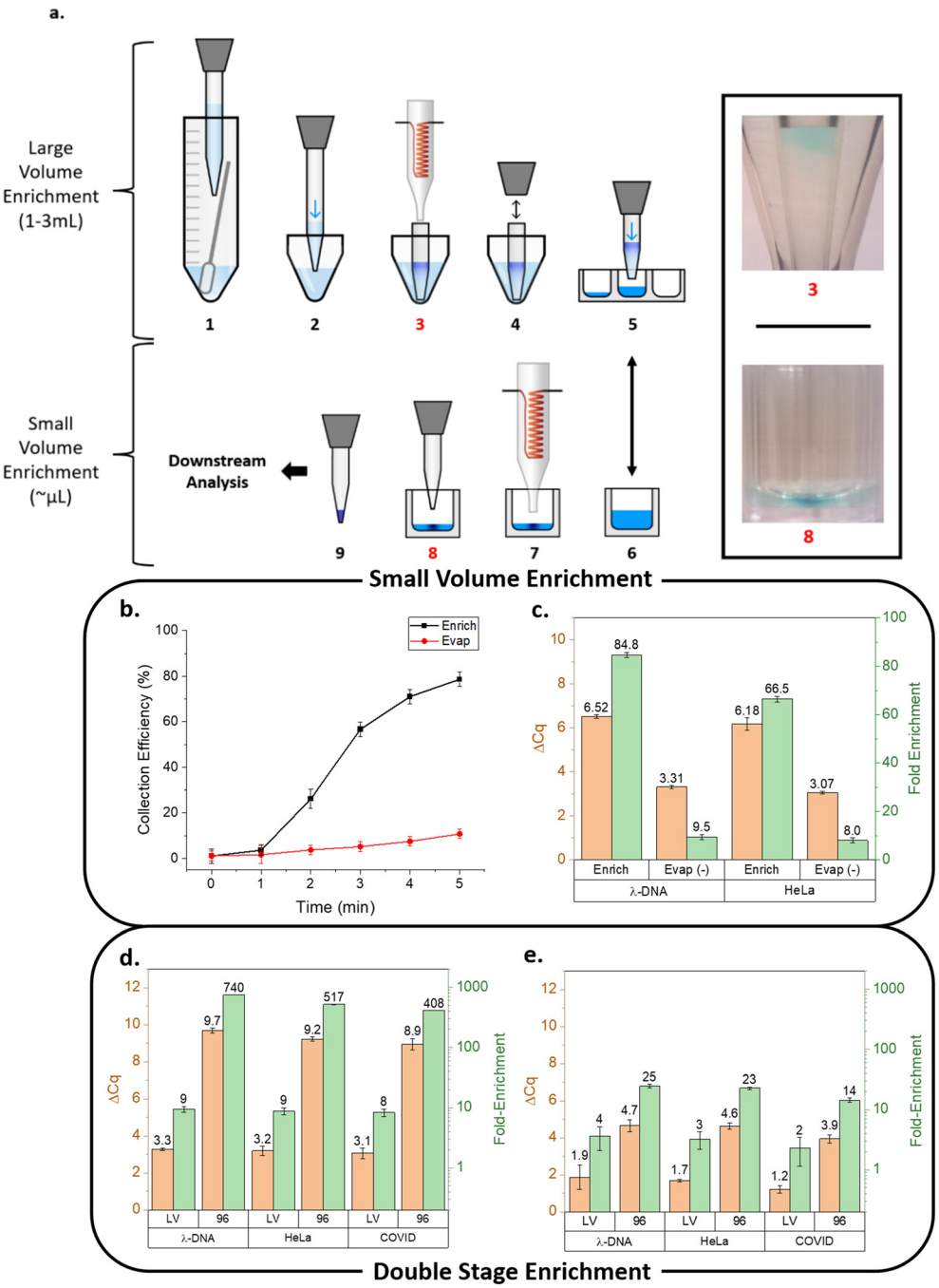

Fig. 5 (a) Diagram of the two-stage enrichment process with images from certain steps labeled with red numbers. (b) Collection efficiency *vs.* time for λ-DNA for airjet enrichment (Enrich) and volume reduction (Evap [–]). (c) Comparison of ΔC_q (orange) and collection efficiency (green) for λ-DNA and HeLa-S3 RNA. (d) Cumulative ΔC_q (orange) and fold-enrichment (green) for λ-DNA, HeLa-S3 RNA, and heat-inactivated SARS-CoV-2 after large volume (LV) and small volume (96) enrichment. (e) Cumulative ΔC_q and fold-enrichment for control trials using evaporative reduction only.

tube (Fig. 5a, step 3) where enrichment occurs. The enrichment can be visualized when the tube insert traps and localizes the enriched analytes, as indicated by the blue dye layer from the initially dilute dye solution (Fig. 5a, step 3). The tube insert acts similarly to the stabilizing properties of methyl cellulose, concentrating the enriched fluid while confining the airjet-induced shear forces. Fluid turbulence is more likely to occur due to the larger container dimensions. Introducing a physical barrier raises the turbulence threshold, allowing stronger airflow rates to enhance the evaporation rate significantly. In addition, the inner tube acts as a collection vessel that can be attached to a micropipette to transfer the enriched solution to the next stage (Fig. 5a, steps 4 and 5).

The small-volume enrichment takes place in a 96-well plate and is designed to maximize the enrichment factor for microfluidic volumes. This stage utilizes methyl cellulose as the stabilizing additive and develops a highly concentrated spot after enrichment (Fig. 5a, step 8). The effectiveness of airjet enrichment over conventional evaporative volume reduction is shown in Fig. 5b by tracking the collection efficiency for a λ-DNA solution over time. The collection efficiency is determined through qPCR by comparing the C_q values from 1 μL of the initial, unenriched sample with 1 μL of the sample undergoing enrichment. The ΔC_q between these two samples is used to determine the percentage of functional analytes collected at the end of the sample preparation process (*i.e.*, the end-to-end efficiency). In this method, airjet enrichment with methyl cellulose surfactant captured 80% of λ-DNA in 1 μL volume from a 100 μL sample. In comparison, volume reduction by evaporation results in less than 10% of the λ-DNA in the 1 μL transferred volume. The difference is that the airjet-enrichment method localizes the analyte underneath the nozzle for easy and efficient sample extraction or transfer. In contrast, evaporative volume reduction produces a uniform analyte distribution within the remaining volume and suffers from the coffee-ring effect.

In addition to DNA, RNA is a frequently targeted analyte for detection but is more susceptible to degradation. Therefore, the collection efficiencies of HeLa-S3 RNA were evaluated alongside λ-DNA to determine if airjet enrichment was equally effective (Fig. 5c). Upon comparison, RNA results yielded consistently lower collection efficiencies averaging to 67%, while λ-DNA exhibited a 85% average collection efficiency. The reduced efficiency observed for RNA may be attributed to temperature-dependent auto-hydrolysis caused by the heated airjet. According to Fig. 4b, a power of 1.9 W used during RNA enrichment would yield a mild temperature profile (between 16 and 22 °C). However, this profile measurement was taken with a filled well containing 350 μL of liquid. It is likely that during the latter stages of RNA enrichment, the reduced fluid volume of ~20 μL lowered the overall heat capacity and led to increased temperatures. Although RNA enrichment did not usually achieve the same collection efficiency as DNA, the efficiency is still far greater than that of the evaporated control sample.

To evaluate the effectiveness of the proposed workflow (Fig. 5a) in improving detection sensitivity, the large and small volume enrichment stages were combined and tested for three analytes: λ-DNA, HeLa-S3 RNA, and heat-inactivated SARS-CoV-2. Cumulative ΔC_q and fold-enrichment values after each enrichment stage are shown in Fig. 5d. These values reflected the performance for each step concerning the optimization of fluid reduction and enrichment effectiveness. For the large volume stage, the enrichment could consistently reduce the C_q by an average of 3.17 cycles regardless of the nucleic acid tested. More importantly, this step could evaporate off more than 1 mL of fluid and condense the analytes into 100 μL for transfer. The small volume enrichment step then significantly reduced the overall C_q by an average of 9.27 cycles within minutes. Among the analytes, λ-DNA exhibited the highest ΔC_q and fold-enrichment at 9.67 and 740-fold, respectively, while SARS-CoV-2 had the lowest values at 8.94 and 408-fold enrichment. RNA enrichment generally yielded lower values, consistent with the findings in Fig. 5c, and analyte loss occurred primarily during the small-volume enrichment stage. These cumulative values can be compared to the control trials in Fig. 5e, where the large volume stage lacked the inner tube, and the small volume stage did not include the methyl cellulose, thereby solely relying on volume reduction to achieve enrichment. Based on this difference, the airjet enrichment stages demonstrate considerable advantages in achieving analyte enrichment.

Selective analyte enrichment in high salt buffers

While the double-stage enrichment significantly improved the overall detection sensitivity, the experiment was performed in non-buffered solutions. However, many available storage solutions contain specific salts to prevent early degradation of the analyte – often in much higher concentrations than the analyte itself. While a merit of the airjet enrichment is the ability to enrich a wide range of substances, the co-enrichment of unwanted elements, particularly salt, could adversely interfere with downstream analyses or even damage the analytes. Co-enrichment of specific substances could therefore be used to create a distinct environment of limited salt solubility, and prevent salt accumulation during the analyte enrichment process. PEG_{400}, a non-volatile compound in which salts have demonstrated reduced solubility,[38] was added in each sample to determine whether it could decrease salt co-enrichment. The double-stage enrichment was repeated with the same analytes spiked in a solution of 5% (v/v) PEG_{400} and 0.1 mM EDTA. EDTA is a chelator for divalent cations and a commonly used salt for RNA storage. However, it is also a PCR inhibitor at high concentrations as it sequesters the magnesium ions which are cofactors for polymerase activity. Co-enrichment of PEG_{400} was examined to the degree by which it could reduce the ΔC_q and recover the signal during downstream analysis.

The cumulative enrichment values for λ-DNA, HeLa-S3 RNA, and heat-inactivated SARS-CoV-2 in 0.1 mM EDTA are shown in (Fig. 6). The EDTA concentration threshold for qPCR functionality was determined to be 15 mM when withdrawing 1 μL of sample (Fig. S5†). The effect of EDTA accumulation in the downstream analysis is exemplified in the negative controls without PEG. While a qPCR signal was obtained after the large volume stage, the co-enrichment in the 96-well plate led to a high enough EDTA concentration to inhibit the PCR reaction – thereby leading to no signal. However, upon the addition of a 5% PEG solution to the 96-well stage, recovery of the qPCR signal as well as enrichment, was seen for all samples. Using the final λ-DNA fold-

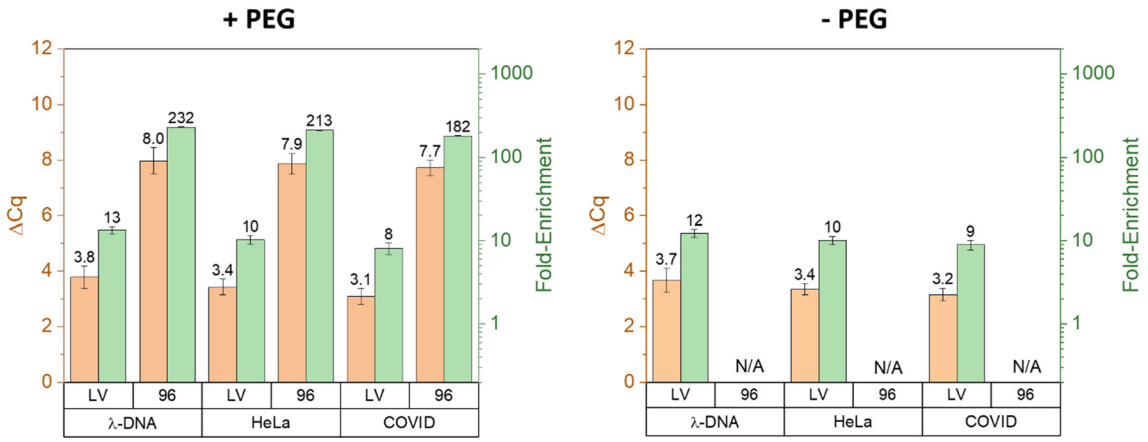

Fig. 6 Comparison of cumulative ΔC_q (orange) and fold-enrichment (green) for λ-DNA, HeLa-S3 RNA, and heat-inactivated SARS-CoV-2 in 0.1 mM EDTA for solutions with PEG (+ PEG) and without PEG (– PEG).

enrichment value of 232, it can be assumed that the same amount would also concentrate the EDTA if PEG was absent – crossing the 15 mM threshold and resulting in no qPCR signal. Therefore, the presence of a signal indicates PEG has some desalting capabilities.

The final ΔC_q values were lower in the buffered samples than those in the non-buffered samples. The addition of PEG caused this reduction, as it may mildly interfere with the function of methyl cellulose as a surfactant to suppress turbulence. Consequently, the enrichment efficiency is decreased as fluid turbulence becomes more prevalent in disrupting the formation of the enrichment spot. Therefore, while adding PEG reduces the co-enrichment of salt, it also disrupts the airflow-based CRE reversal to a certain degree. In addition, it was found that higher concentrations of PEG led to inhibition of the PCR reaction in both DNA and RNA based assays (Fig. S6†). Therefore, although PEG successfully recovered and increased the signal from EDTA accumulation, the enrichment of PEG itself resulted in suboptimal performance in both the enrichment and qPCR results. Future studies that screen for alternative compounds that minimize this trade-off would thus be beneficial.

Airjet enrichment in ELISA

Airjet enrichment was employed in a preliminary sandwich ELISA experiment to assess the fold-enrichment capabilities using rabbit IgG as a model antigen (Fig. 7a). The enrichment of protein analytes poses a greater challenge as buffers with consistent salt concentrations are needed to preserve protein structure. To determine the effectiveness of enrichment, a comparison was made between a solution containing methyl cellulose (Enrich in Fig. 7a) and a negative control without methyl cellulose (Evap in Fig. 7a), where the former was anticipated to undergo spot enrichment while the latter was expected to evaporate uniformly.

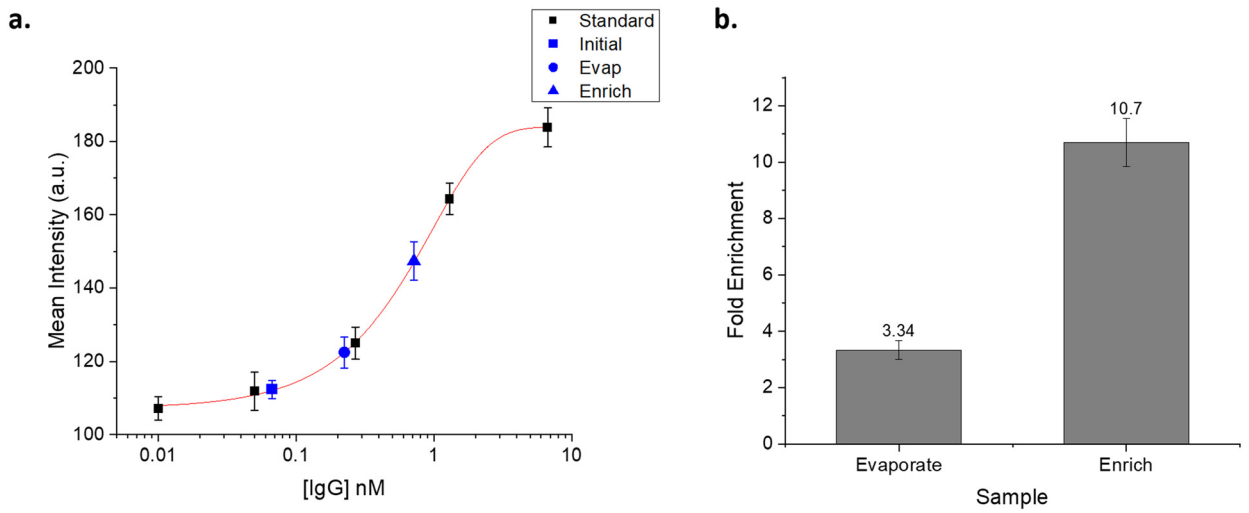

Fig. 7 (a) Standard curve of ELISA assay (black) and respective concentrations of initial, evaporated, and enriched samples (blue). (b) Fold-enrichment values of evaporated and enriched samples.

Although both samples improved the sensitivity of the assay, the fold-enrichment was lower than expected for each case (Fig. 7b), especially when compared to nucleic acid enrichment. In both cases, the salt concentration increases during antigen enrichment, which could potentially lead to its denaturation prior to binding with the capture antibody. Furthermore, in the enriched samples, the co-enrichment of salt may lead to the formation of density gradients that promote fluid flow, thereby disrupting the enrichment spot and impeding solute localization. Despite, the enriched sample enhancing the assay's sensitivity in comparison to the evaporated sample, this outcome may vary depending on the protein and its sensitivity to changes in salt concentration. Therefore, it is important to consider the interference of salt when determining the suitability of airjet enrichment in specific applications.

Conclusion

In summary, we report an airjet enrichment method that can concentrate analytes to aid in sample preparation and improve downstream detection sensitivity. The method is simple, requiring only compressed air, a nozzle, and a surfactant. As airjet enrichment relies on reversing the coffee-ring effect, various particles and molecules can be concentrated regardless of their physical and chemical properties. The degree of enrichment was quantified using qPCR with λ-DNA, HeLa-S3 RNA, and heat-inactivated SARS-CoV-2 acting as model analytes. CRE reversal found that over 70% of λ-DNA and HeLa-S3 RNA could be localized to a 1 μL volume for transfer. A workflow was described to adapt the enrichment method to accommodate larger volumes typically seen in nucleic acid sample preparation protocols. The modified workflow resulted in a substantial reduction in C_q, averaging 9.27 across all model analytes. Furthermore, adding PEG to buffered solutions allowed for selective enrichment by preventing the co-enrichment of salts and recovering a qPCR signal previously lost due to salt interference. The simplicity and effectiveness of the airjet enrichment method make it easily applicable to various common assays, as well as a complementary technique for existing sample preparation methods. While this study focused primarily on nucleic acids, airflow enrichment was also utilized in ELISA as an initial demonstration to enhance protein sensitivity. Although there are additional considerations to be addressed, airjet enrichment exhibits versatile applicability to a range of chemical and biological analytes, offering improved detection capabilities.

Conflicts of interest

The authors declare that they do not have any competing financial interests or specific relationships that could have appeared to influence the work reported in this paper.

Acknowledgements

The project was partially supported from funding under IARPA Contract 2020-20090400002.

References

1 C. C. Lin, J. L. Hsu and G. Bin Lee, *Microfluid. Nanofluid.*, 2010, **10**(3), 481–511.
2 B. C. Giordano, D. S. Burgi, S. J. Hart and A. Terray, *Anal. Chim. Acta*, 2012, **718**, 11–24.
3 M. Shen, Y. Zhou, J. Ye, A. A. Abdullah Al-maskri, Y. Kang, S. Zeng and S. Cai, *J. Pharm. Anal.*, 2020, **10**, 97–101.
4 Z. Li, X. Xu, D. Wang and X. Jiang, *TrAC, Trends Anal. Chem.*, 2023, **158**, 116871.
5 B. S. Broyles, S. C. Jacobson and J. M. Ramsey, *Anal. Chem.*, 2003, **75**, 2761–2767.
6 C. Yu, M. H. Davey, F. Svec and J. M. J. Fréchet, *Anal. Chem.*, 2001, **73**, 5088–5096.
7 S. Dadfarnia and A. M. Haji Shabani, *Anal. Chim. Acta*, 2010, **658**, 107–119.
8 H. Shen, Q. Fang and Z. L. Fang, *Lab Chip*, 2006, **6**, 1387–1389.
9 K. Sueyoshi, F. Kitagawa and K. Otsuka, *J. Sep. Sci.*, 2008, **31**, 2650–2666.
10 A. Manz, D. J. Harrison, E. M. J. Verpoorte, J. C. Fettinger, A. Paulus, H. Lüdi and H. M. Widmer, *J. Chromatogr. A*, 1992, **593**, 253–258.
11 T. Tsuda, K. Nomura and G. Nakagawa, *J. Chromatogr. A*, 1982, **248**, 241–247.
12 E. Fornells, E. F. Hilder and M. C. Breadmore, *Anal. Bioanal. Chem.*, 2019, **411**, 1715–1727.
13 P. Bacchin, J. Leng and J. B. Salmon, *Chem. Rev.*, 2022, **122**, 6938–6985.
14 M. Yang, D. Chen, J. Hu, X. Zheng, Z. J. Lin and H. Zhu, *TrAC, Trends Anal. Chem.*, 2022, **157**, 116752.
15 J. L. Garcia-Cordero and Z. H. Fan, *Lab Chip*, 2017, **17**, 2150–2166.
16 H. Hu and R. G. Larson, *J. Phys. Chem. B*, 2006, **110**, 7090–7094.
17 D. Mampallil and H. Burak Eral, *Adv. Colloid Interface Sci.*, 2018, **252**, 38–54.
18 H. Y. Erbil, *Adv. Colloid Interface Sci.*, 2012, **170**, 67–86.
19 R. D. Deegan, O. Bakajin, T. F. Dupont, G. Huber, S. R. Nagel and T. A. Witten, *Phys. Rev. E: Stat. Phys., Plasmas, Fluids, Relat. Interdiscip. Top.*, 2000, **62**, 756–765.
20 S. J. Kim, K. H. Kang, J. G. Lee, I. S. Kang and B. J. Yoon, *Anal. Chem.*, 2006, **78**, 5192–5197.
21 D. Mampallil, H. B. Eral, D. van den Ende and F. Mugele, *Soft Matter*, 2012, **8**, 10614.
22 J. Zhang, M. K. Borg, K. Ritos and J. M. Reese, *Langmuir*, 2016, **32**, 1542–1549.
23 D. Mampallil, J. Reboud, R. Wilson, D. Wylie, D. R. Klug and J. M. Cooper, *Soft Matter*, 2015, **11**, 7207–7213.
24 R. Shilton, M. K. Tan, L. Y. Yeo and J. R. Friend, *J. Appl. Phys.*, 2008, **104**, 014910.

25 T. M. Yen, X. Fu, T. Wei, R. U. Nayak, Y. Shi and Y. H. Lo, *Sci. Rep.*, 2018, **8**(1), 1–11.
26 F. De Angelis, F. Gentile, F. Mecarini, G. Das, M. Moretti, P. Candeloro, M. L. Coluccio, G. Cojoc, A. Accardo, C. Liberale, R. P. Zaccaria, G. Perozziello, L. Tirinato, A. Toma, G. Cuda, R. Cingolani and E. Di Fabrizio, *Nat. Photonics*, 2011, **5**, 682–687.
27 J. McLane, C. Wu, M. Khine, J. McLane, C. Wu and M. Khine, *Adv. Mater. Interfaces*, 2015, **2**, 1400034.
28 R. G. Larson, *AIChE J.*, 2014, **60**, 1538–1571.
29 H. Hu and R. G. Larson, *J. Phys. Chem. B*, 2002, **106**, 1334–1344.
30 E. Shahraeeni, P. Lehmann and D. Or, *Water Resour. Res.*, 2012, **48**, 9525.
31 E. Wang, Z. Guo, R. Tang and Y. H. Lo, *Lab Chip*, 2021, **21**, 4249–4261.
32 P. Behroozi, K. Cordray, W. Griffin and F. Behroozi, *Am. J. Phys.*, 2007, **75**, 407–414.
33 M. J. Brisco and A. A. Morley, *Nucleic Acids Res.*, 2012, **40**, e144.
34 S. Fleige and M. W. Pfaffl, *Mol. Aspects Med.*, 2006, **27**, 126–139.
35 X. Xu and L. Ma, *Sci. Rep.*, 2015, **5**(1), 1–6.
36 J. R. Trantum, M. L. Baglia, Z. E. Eagleton, R. L. Mernaugh and F. R. Haselton, *Lab Chip*, 2014, **14**, 315–324.
37 T. Still, P. J. Yunker and A. G. Yodh, *Langmuir*, 2012, **28**, 4984–4988.
38 C. W. Kim, J. T. Someren, M. Kirshen and C. Rha, *Phys. Chem. Liq.*, 1988, **18**, 11–20.